




Aggregation States of Poly(4-methylpentene-1) at a Solid Interface

Kentaro Yamamoto¹ · Daisuke Kawaguchi² · Kazuki Sasahara¹ · Manabu Inutsuka¹ · Satoru Yamamoto³ · Kiminori Uchida⁴ · Kazuki Mita⁴  · Hiroki Ogawa⁵ · Mikihiro Takenaka⁵ · Keiji Tanaka^{1,6}

Received: 18 August 2018 / Revised: 20 August 2018 / Accepted: 20 September 2018 / Published online: 7 November 2018
© The Society of Polymer Science, Japan 2018

Abstract

A thin film of poly(4-methylpentene-1) (P4MP1) was prepared on a quartz substrate, which was a model system of an interface in filler-reinforced semicrystalline polymer composites. Grazing-incidence wide-angle X-ray diffraction measurements revealed that P4MP1 in the thin film after isothermal crystallization formed a Form I crystal polymorph composed of a tetragonal unit cell with a 7_2 helix, in which the chain axis was oriented along the direction parallel to the quartz interface. Combining sum-frequency generation vibrational spectroscopy with molecular dynamics simulation enabled us to gain access to the local conformation of P4MP1 chains at the quartz interface and the changes that occurred with isothermal crystallization. Finally, the way in which the initial chain orientation at the substrate interface impacted the crystalline structure in the thin film was discussed.

Introduction

Polymer materials containing a filler such as carbon black, silica particle, or talc, or polymer composites, have been used in a wide variety of technological applications. Many experimental and theoretical studies have hitherto revealed that the physical properties of polymer composites are dependent on to what extent the filler is fed and how it is dispersed [1–28]. Additionally, in the case of composite materials using a semicrystalline polymer, the filler generally plays an additional role as a nucleating agent [29–31]. When

glass fiber was mixed into polyolefin, a transcrystalline phase was formed in the interfacial region [32, 33]. Additionally, a peculiar crystalline phase was formed in a polypropylene/silica nanocomposite [34]. Thus, the aggregation states of semicrystalline chains at an inorganic solid interface are of pivotal importance to obtain a better understanding of polymer composites.

Sum-frequency generation (SFG) vibrational spectroscopy is one of the most powerful tools to examine the interfacial aggregation states of polymer chains and provides the best depth resolution among the available techniques [35–38]. We have applied this technique to study the local conformation of polystyrene, poly(methyl methacrylate), polyisoprene and styrene-butadiene rubbers in films at interfaces with inorganic solids [39–47]. As a general trend, when a thin film is prepared on a solid substrate by the spin-coating method, the chains are aligned in-plane at the substrate interface mainly due to centrifugal force [42, 43, 46, 47]. Additionally, the thermal relaxation of the chains at the substrate interface is difficult to attain even at a temperature higher than the bulk glass transition temperature (T_g) [42, 43, 46, 47]. Such relaxation is challenging because the chain dynamics are much slower in the interfacial region than in the bulk [48–52].

When SFG is applied to a film with clear interfaces, signals can be generated from the internal interfacial regions in addition to the air and substrate interfaces because the centrosymmetry at such internal interfaces is also broken. This is the case for semicrystalline polymers such as crystalline β -chitin [53], cellulose [54], collagen [55] and poly

✉ Daisuke Kawaguchi
kawaguchi@molecular-device.kyushu-u.ac.jp

✉ Keiji Tanaka
k-tanaka@cstf.kyushu-u.ac.jp

¹ Department of Applied Chemistry, Kyushu University, Fukuoka 819-0395, Japan

² Education Center for Global Leaders in Molecular Systems for Devices, Kyushu University, Fukuoka 819-0395, Japan

³ Dassault Systèmes K.K., Tokyo 141-6020, Japan

⁴ Mitsui Chemicals Inc., Chiba 299-0265, Japan

⁵ Institute for Chemical Research, Kyoto University, Uji 611-0011, Japan

⁶ International Institute for Carbon-Neutral Energy Research (WPI-I2CNER), Kyushu University, Fukuoka 819-0395, Japan

(lactic acid) [56]. In addition, for a noncentrosymmetric unit cell, the transition dipoles of molecular vibrations possess net polar ordering within individual crystallites [53]. This ordering leads to unique selection rules, which are useful determining chain packing in a bulk crystalline phase with low symmetry. However, this feature can be a disadvantage for the characterization of semicrystalline polymers at the air and substrate interfaces. Thus, when SFG is applied to semicrystalline polymers, it is necessary to consider where the signals are generated from.

Here we examine the local conformation of a semicrystalline polymer, poly(4-methylpentene-1) (P4MP1) [57], in a film at the interface with a quartz substrate by SFG in conjunction with atomistic molecular dynamics (MD) simulation. Using grazing-incidence wide-angle X-ray diffraction (GIWAXD) measurements, way in which the interfacial structure impacts the crystalline structure and orientation of P4MP1 in the thin film is also discussed.

Experimental section

Materials

As a material, isotactic P4MP1 supplied by Mitsui Chemicals, Inc. Chiba, Japan was used. The weight-averaged molecular weight and polydispersity index were previously determined to be 270 k and 3.2, respectively, by gel permeation chromatography with polystyrene standards. The melting temperature of P4MP1 was 513 K by differential scanning calorimetry (DSC6220, SII Nanotechnology Inc.) with a heating rate of 10 K•min⁻¹. Films of P4MP1 for GIWAXD and SFG were prepared by dip-coating and spin-coating methods, respectively, from a *p*-xylene solution kept above 383 K onto quartz prisms, quartz windows and Si wafers kept above 373 K. The quartz substrates were cleaned by a piranha solution, i.e., a mixture of H₂SO₄ and H₂O₂ (70/30 v/v), at 363 K for 2 h. Then, the substrates were thoroughly rinsed in deionized water and dried by nitrogen. The silicon wafers were cleaned by irradiation by vacuum ultraviolet (VUV) light for 10 min at room temperature under 50 Pa. A P4MP1 film was partly scratched by a blade, and the step height between the film and substrate surfaces was examined by atomic force microscopy (AFM). The resulting value was postulated to be the film thickness. To prepare a film sandwiched between quartz substrates for SFG, two films prepared on a quartz prism and window were attached together in face-to-face geometry at 533 K. The films for GIWAXD measurements were isothermally crystallized at 473 K for 2 h under vacuum. The films for SFG measurements were melted at 533 K and isothermally crystallized at 500 K for 2 h in a N₂ atmosphere.

Characterization

The crystalline structure of P4MP1 in a thin film was discussed on the basis of GIWAXD measurements performed on the BL03XU beamline at SPring-8, Japan [58, 59]. The incidence angle of the X-rays with a wavelength (λ) of 0.1 nm was chosen to be 0.14°, which was larger than the corresponding critical angle of 0.09°. Thus, the diffraction pattern so obtained reflects the internal structure of the film. A sector-averaged diffraction pattern was obtained from a two-dimensional GIWAXD pattern as a function of scattering vector q ($= 4\pi\sin\theta_s/\lambda$), where $2\theta_s$ is the scattering angle.

The aggregation states of P4MP1 in a film at the substrate interface were examined by SFG. The visible beam with a wavelength of 532 nm was generated by frequency-doubling the fundamental output pulses from a picosecond Nd:YAG laser (PL2250-10-B, EKSPLA). The tunable infrared (IR) beam was generated from an EKSPLA optical parametric generation/amplification and difference frequency generation system based on LBO and AgGaS₂ crystals. SFG spectra were collected with visible and IR beams traveling through the prism and overlapping at the center of the sample. The incident angles of the visible and IR beams were 55° and 65° from the surface normal, respectively. The intensity of the SFG signal (I_{SFG}) is proportional to the square of the absolute value of the effective sum-frequency susceptibility tensor of the interface ($\chi_{\text{eff}}^{(2)}$):

$$I_{\text{SFG}} \propto \left| \chi_{\text{eff}}^{(2)} \right|^2 I_{\text{vis}} I_{\text{IR}} \quad (1)$$

where I_{vis} and I_{IR} are the intensities of visible and IR lasers, respectively. Thus, the SFG intensity was normalized to those of the original visible and IR beams. Here, $\chi_{\text{eff}}^{(2)}$ can be described by the following equation:

$$\chi_{\text{eff}}^{(2)} = \chi_{\text{NR}}^{(2)} + \sum_q \frac{A_q}{\omega_{\text{IR}} - \omega_q + i\Gamma_q} \quad (2)$$

where $\chi_{\text{NR}}^{(2)}$ originates from the nonresonant background. A_q , ω_q and Γ_q are the peak intensity, resonant frequency and damping coefficient, respectively, for the q^{th} vibrational mode. The peak intensity of each component was determined by curve-fitting using Eqs. 1 and 2. The measurements were carried out at room temperature with the *ssp* (SF output, visible input, and infrared input) polarization combination.

The interfacial aggregation states of P4MP1 were also validated through MD simulations using the software package Materials Studio 2017R2 (Dassault Systèmes). The density of isotactic P4MP1 with a degree of polymerization of 150 was calculated to be 0.82 g•cm⁻³ based on MD simulations with the canonical NPT ensemble in the bulk. Then, P4MP1 chains were filled into an amorphous cell, which was structurally optimized for 1 ns in the canonical

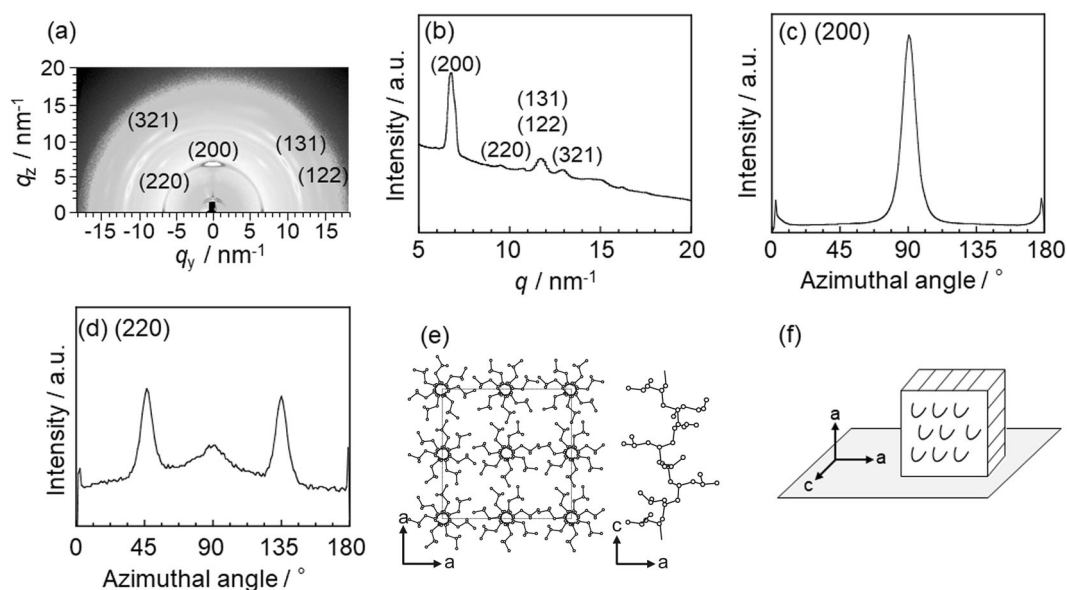


Fig. 1 (a) A two-dimensional GIWAXD pattern, (b) a sector-averaged one-dimensional GIWAXD pattern from 0° to 180° and azimuthal plots for (c) (200) and (d) (220) diffractions for a P4MP1 film. (e) A

unit cell for the Form I polymorph of P4MP1. (f) Schematic representation of the crystalline orientation in the P4MP1 film

NVT ensemble. A shear rate of $4 \text{ nm} \cdot \text{ps}^{-1}$ was applied to the P4MP1 chains to create an initial chain conformation. To model the quartz surface, a SiO_2 lattice was first derived from the structural database. A repeating unit of SiO_2 was cleaved along the (001) crystallographic orientation, leading to the formation of a surface consisting of oxygen. Then, unsaturated oxygen atoms at the surface were capped by hydrogen atoms. Next, a vacuum slab with a thickness of 5 nm was created between the two surfaces to fill two chains in the space so that the lattice size was $3 \text{ nm} \times 3 \text{ nm}$ in the xy -plane and 5 nm along the z -axis. Finally, the polymer layer formed in the amorphous cell was placed between the SiO_2 surfaces to produce the initial construction. The MD simulations were conducted in the following two steps by the Forcite module using the PCFF force field [60, 61]. First, the system was evolved at 537 K for 1 ns so that the chains could be easily moved to promote the relaxation process. Second, the system was aged at 298 K for 1 ns for analysis of the steady state. The integration step was set to 0.5 fs. A Berendsen loose-coupling thermostat was chosen for finite temperature control of the system. Van der Waals and electrostatic interactions were calculated using a group-based method, and the cut-off distance was 1.25 nm.

Results and discussion

Crystalline structure in the thin films

Figure 1a, b show a two-dimensional GIWAXD pattern for a P4MP1 thin film with a thickness of $\sim 100 \text{ nm}$ and

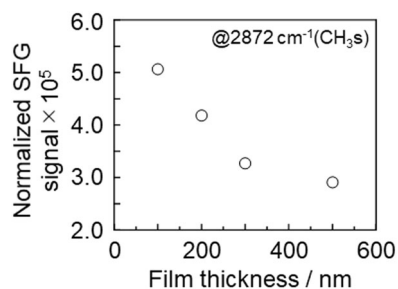
a sector-averaged diffraction intensity from panel (a), respectively. Diffraction peaks were observed at q values of 6.7, 9.5, 11.5 and 13.0 nm^{-1} . It has been reported that P4MP1 shows the so-called crystalline polymorphic phases Forms I, II, III and IV [57, 62–67]. Table 1 collects data reported by Tadokoro considering the crystalline structures, typical hkl Miller indices and corresponding q values of the reflections in the X-ray diffraction patterns for P4MP1 [57, 62–67]. Comparing our data shown in Fig. 1b with Table 1, it can be claimed that P4MP1 in the thin film formed the Form I phase, which was composed of a tetragonal unit cell with $a = 1.87 \text{ nm}$ and $c = 1.38 \text{ nm}$. Panels (c) and (d) of Fig. 1 show azimuthal plots for (200) and (220) extracted from Fig. 1a. While (200) diffraction was predominantly observed at 90° , (220) diffraction was observed at 45° and 135° . This means that (200) and (220) were oriented parallel to the surface and diagonal in the aa -plane of a tetragonal unit, respectively, as shown in Fig. 1e, f. In this case, the c -axis, or fiber axis, is parallel to the surface. The crystalline orientation and the aggregation states of the chains at the substrate interface are discussed in a later section using SFG in conjunction with MD simulation.

Local conformation at the quartz interface

It was first confirmed whether SFG signals were generated from the internal regions of the P4MP1 film. Tadokoro, using XRD, also reported that the space group for Form I of P4MP1 is $P\bar{4}b2$ [43]. This is a centrosymmetric space group, which possesses eight general equivalent positions,

Table 1 Crystalline structure of P4MP1 reported by Tadokoro considering typical hkl Miller indices and the corresponding q values in X-ray diffraction patterns

Form I 7_2 helix, tetragonal ($a = 1.866$, $c = 1.380$ nm)		Form II 4_1 helix, monoclinic ($a = 1.049$, $b = 1.889$, $c = 0.713$ nm, $\gamma = 113.7^\circ$)		Form III 4_1 helix, tetragonal ($a = 1.946$, $c = 0.702$ nm)		Form IV 3_1 helix, hexagonal ($a = 2.217$, $c = 0.65$ nm)	
(hkl)	q / nm^{-1}	(hkl)	q / nm^{-1}	(hkl)	q / nm^{-1}	(hkl)	q / nm^{-1}
200	6.72	100	6.54	200	6.47	110	5.73
220	9.50	020	7.32	220, 101	9.17	200	6.69
131	11.58	$\bar{1}20$	7.71	211	11.50	210	8.60
122	11.87	011	9.38	400, 301	12.98	310	11.64
321	12.96	$\bar{1}\bar{1}1$	10.55	420, 321	14.63	211	12.91
		021	11.57				
		111	12.20				
		200	12.94				

**Fig. 2** Thickness dependence of the SFG intensity at $2,872 \text{ cm}^{-1}$ corresponding to the symmetric C–H stretching vibration of methyl groups (CH_3s)

a glide plane and 4-fold rotoinversion symmetry. On the other hand, SFG signals can be generated at interfaces where the centrosymmetry of the space is broken. Thus, it seems likely that SFG signals are not generated from the internal bulk region of the P4MP1 film. To confirm this hypothesis and to judge which interface was primarily probed, the intensity of the SFG signals from the P4MP1 film was examined as a function of thickness. To regulate the film thickness as desired, a spin-coating method was applied here. Figure 2 shows the result for SFG signal at 2872 cm^{-1} , corresponding to the symmetric C–H stretching vibration of methyl groups (CH_3s), as shown in Fig. 3. The intensity decreased with increasing film thickness. As the P4MP1 film thickness increased, the absorption of the IR beam in the film increased, resulting in a decrease in the intensity of the SFG signal from the interface located on the side opposite that where excited light enters. Thus, Fig. 2 supports our hypothesis that the SFG signals generated from the internal region of the P4MP1 film are trivial, if any.

Figure 3a shows an SFG spectrum with the ssp polarization combination for an as-spun P4MP1 film with a total thickness of approximately 400 nm. Open circles denote experimental data, and dotted curves are lines of best-fit obtained using Eqs. 1 and 2. A solid curve is the sum of dotted curves. Following the aforementioned discussion, it can be claimed that the origin of the spectrum is P4MP1 at the quartz interface. The peaks observed at 2847 and 2935 cm^{-1} were assigned to the symmetric and antisymmetric C–H stretching vibrations of methylene groups (CH_2s and CH_2as) [68]. The peaks at 2872 and 2967 cm^{-1} were assigned to the symmetric and antisymmetric C–H stretching vibrations of methyl groups (CH_3s and CH_3as) [68]. A peak observed at 2908 cm^{-1} seems to be from the C–H stretching vibration of methyne groups [68].

To discuss the local conformation of P4MP1 at the substrate interface, isopropyl groups ($-\text{C}(\text{CH}_3)_2$) are examined here. The SFG intensity is the square of the second-order nonlinear optical susceptibility, which is related to the molecular hyperpolarizability components through the molecular orientation. An isopropyl group in which two CH_3 groups exist and are connected to the same carbon atom possesses C_{2v} symmetry. Additionally, CH_3 groups have C_{3v} symmetry. A vector ν , which bisects the two CH_3 groups, was used to describe the molecular orientation of the isopropyl group [69–71]. The angle between the principal axis of each methyl group and the vector ν , i.e., angle α , is defined to be 54.7° . The tilt and twist angles, θ and Ψ , of vector ν are defined as shown in Fig. 3b. The azimuthal angle ϕ of each CH_3 group is also defined in Fig. 3b. Assuming that the sample is isotropic in the x – y plane and the azimuthal angle can be averaged, the second-order nonlinear susceptibility components of the C–H stretching

Fig. 3 (a) An SFG spectrum with *ssp* polarization combination for an as-spun P4MP1 film. (b) A schematic representation of three angles to define the orientation of an isopropyl group. (c) SFG intensity ratios of symmetric to antisymmetric C–H stretching modes for CH₃ groups (I_s/I_{as}) as functions of θ and ψ

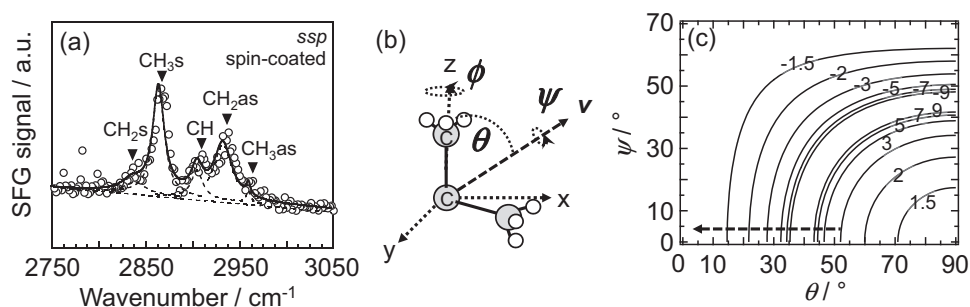
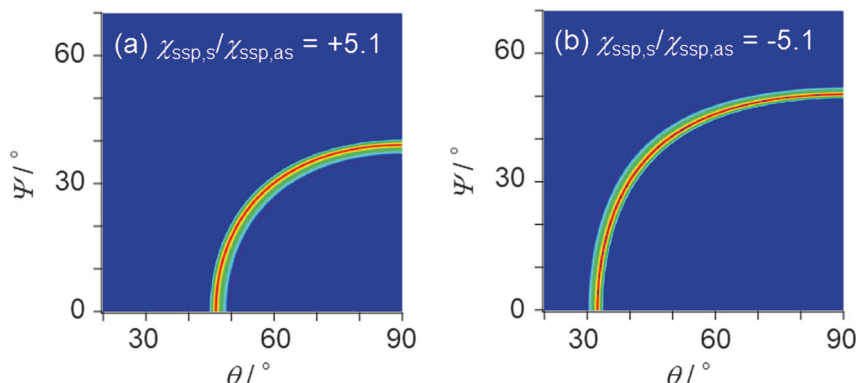


Fig. 4 Heat maps for possible θ and ψ values of isopropyl groups at $\chi_{ssp,s}/\chi_{ssp,as}$ values of (a) 5.1 and (b) -5.1



mode for the isopropyl groups in the lab-fixed coordination system ($\chi_{xxz,s}$, $\chi_{yyz,s}$, $\chi_{xxz,as}$, $\chi_{yyz,as}$) can be described as:

$$\chi_{yyz,s} = \chi_{xxz,s} = \frac{N}{2\epsilon_0} (\beta_{aac} - \beta_{ccc}) \left\{ (\cos \theta - \cos^3 \theta) \left[(5 + 3 \cos 2\psi) (\cos \alpha - \cos^3 \alpha) - 2 \cos \alpha \right] - 2 \cos \theta (\cos \alpha - \cos^3 \alpha) \right\} + \frac{2N}{\epsilon_0} \beta_{aac} \cos \theta \cos \alpha \quad (3)$$

$$\chi_{yyz,as} = \chi_{xxz,as} = \frac{N}{\epsilon_0} \beta_{caa} \left\{ [-2 \cos \theta + 3(\cos \theta - \cos^3 \theta)(1 + \cos 2\psi)] \times (\cos \alpha - \cos^3 \alpha) - 2(\cos \theta - \cos^3 \theta) \cos^3 \alpha \right\} \quad (4)$$

where N is the number density of functional groups detected at the interface, ϵ_0 is the permittivity of free space, and β_{aac} , β_{ccc} , and β_{caa} are the hyperpolarizability components of the C–H stretching mode of a single CH₃ group. β_{aac} , β_{ccc} , and β_{caa} values of 2.3, 1 and 2.3, respectively, were used here [71, 72].

Figure 3c shows the calculated $\chi_{ssp,s}/\chi_{ssp,as}$ values as functions of θ and ψ . The $\chi_{ssp,s}/\chi_{ssp,as}$ value can be either positive or negative depending on the combination of θ and ψ . When θ is larger than 41° and ψ is smaller than 44° , i.e., in the right-bottom corner region of Fig. 3c, $\chi_{ssp,s}/\chi_{ssp,as}$ is positive. On the other hand, $\chi_{ssp,s}/\chi_{ssp,as}$ will be negative if the condition is not satisfied. The SFG intensity ratio of CH₃s to CH_{3as} (I_s/I_{as}) for the spin-coated P4MP1 film was

deduced to be 26.3 from Fig. 3a. Since the SFG intensity is the square of the susceptibility ratio, as mentioned above, the experimental $\chi_{ssp,s}/\chi_{ssp,as}$ value was calculated to be ± 5.1 .

Figure 4a, b show heat maps of the possible θ and ψ values for isopropyl groups. In the maps, a red region corresponds to the plausible combinations of θ and ψ for the isopropyl groups. The experimental error was approximately 20%. In the case of the positive $\chi_{ssp,s}/\chi_{ssp,as}$ value ($= +5.1$), the possible θ and ψ ranges were $46^\circ < \theta$ and $\psi < 39^\circ$. On the other hand, in the case of the negative value ($= -5.1$), the possible θ and ψ ranges were $32^\circ < \theta$ and $\psi < 50^\circ$. Which calculation is more plausible is discussed in the later section.

Conformational change at the interface upon isothermal crystallization

We finally come to the conformational change in P4MP1 at the quartz interface upon isothermal crystallization. Figure 5 shows SFG spectra for the spin-coated P4MP1 film annealed at 500 K for different times. For comparison, a spectrum before isothermal crystallization, which corresponds to Fig. 3a, is also shown. The peak for CH_{3as} disappeared at $t = 15$ min and then appeared at $t = 45$ min. That is, once the I_s/I_{as} value increased to infinity after $t = 15$ min, I_s/I_{as} decreased to 10.5 and 3.0 at $t = 45$ and 120 min, respectively. Since the $\chi_{ssp,s}/\chi_{ssp,as}$ value can be

either positive or negative, as shown in Fig. 3c, the change in the I_s/I_{as} value will be explained in terms of an increase or a decrease in θ . However, since the quantitative determination of θ is experimentally difficult, MD simulations were carried out.

Figure 6a, b show a snapshot of the local conformation of P4MP1 in a film and the θ distribution for the isopropyl groups. Postulating that the chains in the simulation cell were well relaxed, as mentioned in the experimental section, the most probable θ value for the chains in a quasi-equilibrium state was estimated to be 17° . This value was smaller than that for the as-cast film, as estimated from Fig. 3c, and suggests that the $\chi_{ssp,s}/\chi_{ssp,as}$ value is negative. Thus, it seems most likely that the change in the I_s/I_{as} value during isothermal crystallization corresponds to a decreasing θ , as shown by a dotted arrow in Fig. 3c. In addition, Fig. 6a shows a ball-and-stick model in which the sizes of chemical bonds are emphasized in comparison with the sizes of atoms. Note that although the polymer density

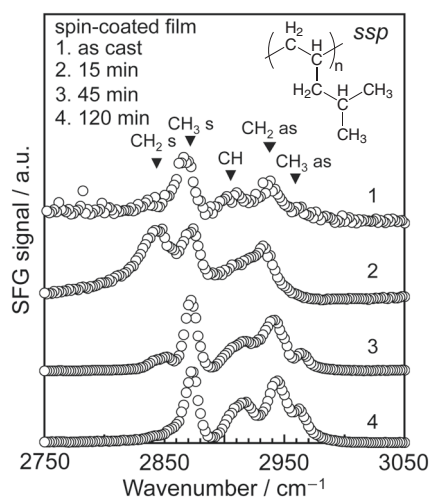


Fig. 5 SFG spectra with *ssp* polarization combination for a spin-coated P4MP1 film after annealing at 500 K, or isothermal crystallization, for various times. For comparison, an SFG spectrum for a corresponding as-cast P4MP1 film is also shown

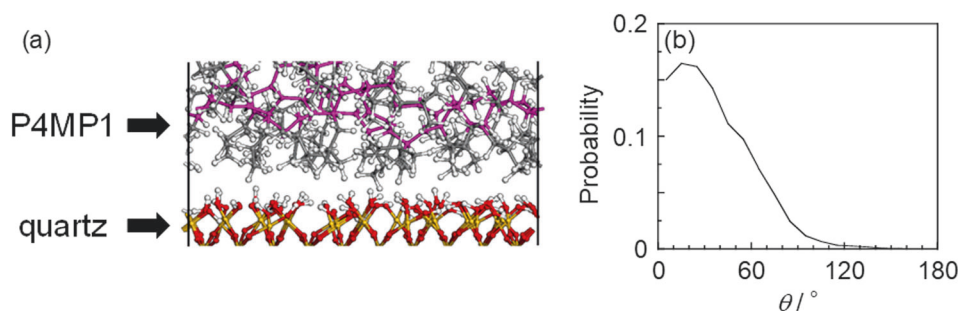


Fig. 6 (a) A snapshot of the local conformation of P4MP1 at the quartz interface after thermal aging for 1 ns. White, gray, red and yellow spheres denote hydrogen, carbon, oxygen and silicon atoms,

appears to be lower at the interface than in the internal region, that is not the case in reality.

The samples for the SFG measurements mentioned above were prepared by the spin-coating method, which was suitable to precisely control the thickness. On the other hand, the sample for the GIWAXD measurement was prepared by the dip-coating method. Since the aggregation states of polymer chains at the interface in a film depend on how the film is prepared [42, 43, 46], the local conformation of a dip-coated P4MP1 film was examined by SFG measurement. Figure 7 shows the SFG spectra with the *ssp* polarization combination for the dip-coated P4MP1 film before and after annealing under the condition of 473 K for 2 h, which is the same as that for the film used in the GIWAXD measurement. The I_s/I_{as} values for the film before and after annealing were 1.41 and 0.90, respectively. That is, the value for the as-dip-coated film was different from that for the as-spin-coated film, corresponding to a $\chi_{ssp,s}/\chi_{ssp,as}$ of -1.19. The negative $\chi_{ssp,s}/\chi_{ssp,as}$ value seems more reasonable, as discussed above. This indicates that the isopropyl groups are more vertically oriented along the direction perpendicular to the interface than are those in the as-spin-coated film. In addition, the I_s/I_{as} value for the dip-coated film decreased with annealing. This trend is in good accordance with that for the spin-coated film.

In the case of P4MP1, unfortunately, the orientation of the main chain part cannot be discussed on the basis of the SFG spectrum because there exist both methylene and methyne groups in the side-chain portion and an isopropyl group is connected to the main chain part via a rotatable C–C bond. The only way to overcome this difficulty is to use MD simulation. In the case of our current MD simulation, a shear force was first applied to the P4MP1 chains, and then the chains were placed in a cell. This model resembles the spin-coating process. Even after aging, the main chain part of P4MP1, which is colored in pink in Fig. 6a, remained oriented along the direction parallel to the quartz interface. This molecular picture obtained by the MD simulation is not inconsistent with the orientational change

respectively. Pink spheres and bonds represent main chain parts. (b) Tilt angle distribution of isopropyl groups at the quartz interface based on MD calculations

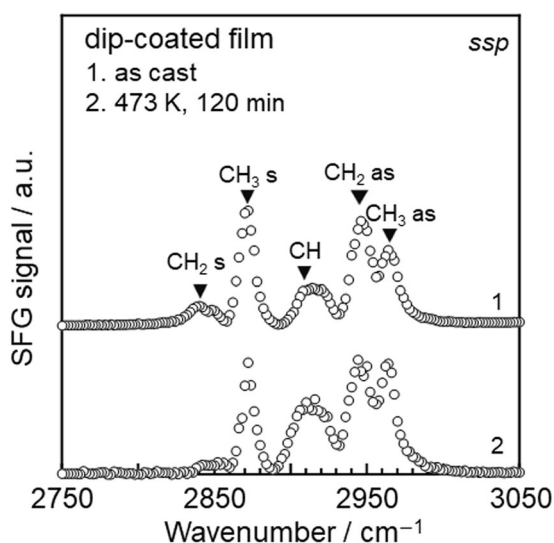


Fig. 7 SFG spectra with the *ssp* polarization combination for a dip-coated P4MP1 film before (as-cast) and after annealing under the condition of 473 K for 2 h, which is the same as that for the sample used in GIWAXD

in the side-chain portion upon isothermal crystallization and is qualitatively consistent with the crystalline structure obtained by the GIWAXD measurements. Taking into account all of the above, it seems reasonable to claim that the orientation of the P4MP1 chains at the substrate interface triggered the formation of the crystal polymorph Form I in the thin film, in which the chain axis was oriented along the direction parallel to the quartz interface.

Conclusions

To obtain a better understanding of the filler effect on the physical properties of polymer composites, a model interface composed of semicrystalline P4MP1 and quartz was structurally characterized in this study. P4MP1 in a thin film on a quartz substrate formed a Form I polymorph with a tetragonal unit cell, in which the fiber axis was oriented along the direction parallel to the quartz interface after isothermal crystallization. Then, interfacial sensitive vibrational spectroscopy was applied to examine the aggregation states of the P4MP1 chains at the quartz interface. Although the orientational information for the side-chain portion of P4MP1 with a depth resolution at a molecular level and the time evolution during the isothermal crystallization process were accessible, the technique was not powerful enough to determine the orientation of the main chain part, which was difficult to distinguish from that of the side-chain part. On the other hand, the atomistic MD simulation could express the orientation of the P4MP1 chain itself in the interfacial region. Our results show how the initial chain orientation of P4MP1 at the quartz interface is important for the

successive formation of the crystalline structure. We believe that this fundamental knowledge will be useful for the design and construction of nanocomposite materials made of semicrystalline polymers.

Acknowledgements This work was partly supported by the Photon and Quantum Basic Research Coordinated Development Program, as well as JSPS KAKENHI for Scientific Research (A) (No. JP15H02183) (KT) and JSPS KAKENHI for Scientific Research (B) (No. JP17H03118) (DK) from the Ministry of Education, Culture, Sports, Science and Technology, Japan. GIWAXD measurements were carried out at BL03XU at SPring-8, constructed by the Consortium of the Advanced Softmaterial Beamline (FSBL) (Proposal No. 2016A7217).

Compliance with ethical standards

Conflict of interest The authors declare that they have no conflict of interest.

References

- Serizawa H, Ito M, Kanamoto T, Tanaka K, Nomura A. Structural-changes during mechanical mixing in carbon black-natural rubber systems studied by pulsed NMR. *Polym J.* 1982;14:149–54.
- Xu CY, Agari Y, Matsuo M. Mechanical and electric properties of ultra-high molecular weight polyethylene and carbon black particle blends. *Polym J.* 1998;30:372–80.
- Du ML, Guo BC, Liu MX, Jia DM. Formation of reinforcing inorganic network in polymer via hydrogen bonding self-assembly process. *Polym J.* 2007;39:208–12.
- Fu SY, Feng XQ, Lauke B, Mai YW. Effects of particle size, particle/matrix interface adhesion and particle loading on mechanical properties of particulate-polymer composites. *Compos Part B-Eng.* 2008;39:933–61.
- Paul DR, Robeson LM. Polymer nanotechnology: Nanocomposites. *Polym (Guildf).* 2008;49:3187–204.
- Zou H, Wu SS, Shen J. Polymer/silica nanocomposites: Preparation, characterization, properties, and applications. *Chem Rev.* 2008;108:3893–957.
- Laoutid F, Bonnaud L, Alexandre M, Lopez-Cuesta JM, Dubois P. New prospects in flame retardant polymer materials: From fundamentals to nanocomposites. *Mater Sci Eng R-Rep.* 2009;63:100–25.
- Lei YD, Tang ZH, Guo BC, Jia DM. SBR/silica composites modified by a polymerizable protic ionic liquid. *Polym J.* 2010;42:555–61.
- Kato M, Usuki A, Hasegawa N, Okamoto H, Kawasumi M. Development and applications of polyolefin- and rubber-clay nanocomposites. *Polym J.* 2011;43:583–93.
- Peng B, Wu H, Bao WT, Guo SY, Chen Y, Huang H, et al. Effects of ultrasound on the morphology and properties of propylene-based plastomer/nanosilica composites. *Polym J.* 2011;43:91–6.
- Liaw WC, Cheng YL, Liao YS, Chen CS, Lai SM. Complementary functionality of SiO₂ and TiO₂ in polyimide/silica-titania ternary hybrid nanocomposites. *Polym J.* 2011;43:249–57.
- Morimune S, Nishino T, Goto T. Poly(vinyl alcohol)/graphene oxide nanocomposites prepared by a simple eco-process. *Polym J.* 2012;44:1056–63.
- Lin CY, Kuo DH, Sie FR, Cheng JY, Liou GS. Preparation and characterization of organosoluble polyimide/BaTiO₃ composite films with mechanical- and chemical-treated ceramic fillers. *Polym J.* 2012;44:1131–7.

14. Fiorentino B, Fulchiron R, Duchet-Rumeau J, Bounor-Legaré V, Majesté J-C. Controlled shear-induced molecular orientation and crystallization in polypropylene/talc microcomposites – effects of the talc nature. *Polym (Guildf)*. 2013;54:2764–75.
15. Ito A, Yasuda T, Ma XF, Watanabe M. Sulfonated polyimide/ionic liquid composite membranes for carbon dioxide separation. *Polym J*. 2017;49:671–6.
16. Joseph N, Varghese J, Sebastian MT. In situ polymerized poly-aniline nanofiber-based functional cotton and nylon fabrics as millimeter-wave absorbers. *Polym J*. 2017;49:391–9.
17. Sivasubramanian G, Hariharasubramanian K, Deivanayagam P, Ramaswamy J. High-performance SPEEK/SWCNT/fly ash polymer electrolyte nanocomposite membranes for fuel cell applications. *Polym J*. 2017;49:703–9.
18. Smith GN, Hallett JE, Joseph P, Tretsiakova-McNally S, Zhang T, Blum FD, et al. Structural studies of thermally stable, combustion-resistant polymer composites. *Polym J*. 2017;49:711–9.
19. Soyama M, Iji M. Improving mechanical properties of cardanol-bonded cellulose diacetate composites by adding polyester resins and glass fiber. *Polym J*. 2017;49:503–9.
20. Yao JY, Zhang SJ, Lim LT, Chen X. Investigation of isothiocyanate release from electrospun modified poly(L-lactic acid)/mustard powder composite fibers. *Polym J*. 2017;49:449–56.
21. Zhang PP, Bin YZ, Zhang R, Matsuo M. Average gap distance between adjacent conductive fillers in polyimide matrix calculated using impedance extrapolated to zero frequency in terms of a thermal fluctuation-induced tunneling effect. *Polym J*. 2017;49:839–50.
22. Lu MZ, Huang S, Chen S, Ju Q, Xiao M, Peng XH, et al. Transparent and super-gas-barrier PET film with surface coated by a polyelectrolyte and Borax. *Polym J*. 2018;50:239–50.
23. Matsuura K, Matsuda Y, Tasaka S. Metastable interface formation in isotactic poly(methyl methacrylate)/alumina nanoparticle mixtures. *Polym J*. 2018;50:375–80.
24. Sakai H, Kuroda K, Muroyama S, Tsukegi T, Kakuchi R, Takada K, et al. Alkylated alkali lignin for compatibilizing agents of carbon fiber-reinforced plastics with polypropylene. *Polym J*. 2018;50:281–4.
25. Sakai R, Teramoto Y, Nishio Y. Producing a magnetically anisotropic soft material: Synthesis of iron oxide nanoparticles in a carrageenan/PVA matrix and stretching of the hybrid gelatinous bulk. *Polym J*. 2018;50:251–60.
26. Tajima T, Tanaka T, Miyake H, Kim IY, Ohtsuki C, Takaguchi Y. Apatite coating on dendrimer-modified buckypaper and the formation of nanoapatite on MWCNTs. *Polym J*. 2018;50:911–7.
27. Tatum WK, Luscombe CK. Pi-conjugated polymer nanowires: Advances and perspectives toward effective commercial implementation. *Polym J*. 2018;50:659–69.
28. Yamamoto T, Norikane Y, Akiyama H. Photochemical liquefaction and softening in molecular materials, polymers, and related compounds. *Polym J*. 2018;50:551–62.
29. Chan-Seok P, Ki-Jun L, Jae-Do N, Seong-Woo K. Crystallization kinetics of glass fiber reinforced PBT composites. *J Appl Polym Sci*. 2000;78:576–85.
30. Okada K, Watanabe K, Urushihara T, Toda A, Hikosaka M. Role of epitaxy of nucleating agent (Na) in nucleation mechanism of polymers. *Polym (Guildf)*. 2007;48:401–8.
31. Pan PP, Liang ZC, Cao A, Inoue Y. Layered metal phosphonate reinforced poly(L-lactide) composites with a highly enhanced crystallization rate. *ACS Appl Mater Interfaces*. 2009;1:402–11.
32. Wang C, Liu CR. Transcrystallization of polypropylene composites: Nucleating ability of fibres. *Polym (Guildf)*. 1999;40:289–98.
33. Assouline E, Pohl S, Fulchiron R, Gérard JF, Lustiger A, Wagner HD, et al. The kinetics of α and β transcrystallization in fibre-reinforced polypropylene. *Polym (Guildf)*. 2000;41:7843–54.
34. Huo H, Jiang S, An L, Feng J. Influence of shear on crystallization behavior of the β phase in isotactic polypropylene with β -nucleating agent. *Macromolecules*. 2004;37:2478–83.
35. Zhu XD, Suhr H, Shen YR. Surface vibrational spectroscopy by infrared-visible sum frequency generation. *Phys Rev B*. 1987;35:3047–50.
36. Shen YR. Surface-properties probed by 2nd-harmonic and sum-frequency generation. *Nature*. 1989;337:519–25.
37. Hirose C, Akamatsu N, Domen K. Formulas for the analysis of surface sum-frequency generation spectrum by CH stretching modes of methyl and methylene groups. *J Chem Phys*. 1992;96:997–1004.
38. Chen Z, Shen YR, Somorjai GA. Studies of polymer surfaces by sum frequency generation vibrational spectroscopy. *Annu Rev Phys Chem*. 2002;53:437–65.
39. Tateishi Y, Kai N, Noguchi H, Uosaki K, Nagamura T, Tanaka K. Local conformation of poly(methyl methacrylate) at nitrogen and water interfaces. *Polym Chem*. 2010;1:303–11.
40. Horinouchi A, Fujii Y, Yamada NL, Tanaka K. Surface reorganization of thin poly(methyl methacrylate) films induced by water. *Chem Lett*. 2010;39:810–1.
41. Horinouchi A, Atarashi H, Fujii Y, Tanaka K. Dynamics of water-induced surface reorganization in poly(methyl methacrylate) films. *Macromolecules*. 2012;45:4638–42.
42. Tsuruta H, Fujii Y, Kai N, Kataoka H, Ishizone T, Doi M, et al. Local conformation and relaxation of polystyrene at substrate interface. *Macromolecules*. 2012;45:4643–9.
43. Inutsuka M, Horinouchi A, Tanaka K. Aggregation states of polymers at hydrophobic and hydrophilic solid interfaces. *ACS Macro Lett*. 2015;4:1174–8.
44. Shimomura S, Inutsuka M, Tajima K, Nabika M, Moritomi S, Matsuno H, et al. Stabilization of polystyrene thin films by introduction of a functional end group. *Polym J*. 2016;48:949–53.
45. Sen M, Jiang N, Cheung J, Endoh MK, Koge T, Kawaguchi D, et al. Flattening process of polymer chains irreversibly adsorbed on a solid. *ACS Macro Lett*. 2016;5:504–8.
46. Sugimoto S, Inutsuka M, Kawaguchi D, Tanaka K. Reorientation kinetics of local conformation of polyisoprene at substrate interface. *ACS Macro Lett*. 2018;7:85–9.
47. Zuo B, Inutsuka M, Kawaguchi D, Wang X, Tanaka K. Conformational relaxation of poly(styrene-co-butadiene) chains at substrate interface in spin-coated and solvent-cast films. *Macromolecules*. 2018;51:2180–6.
48. Wallace WE, Vanzanten JH, Wu WL. Influence of an impenetrable interface on a polymer glass-transition temperature. *Phys Rev E*. 1995;52:R3329–32.
49. Montes H, Lequeux F, Berriot J. Influence of the glass transition temperature gradient on the nonlinear viscoelastic behavior in reinforced elastomers. *Macromolecules*. 2003;36:8107–18.
50. Tanaka K, Tateishi Y, Okada Y, Nagamura T, Doi M, Morita H. Interfacial mobility of polymers on inorganic solids. *J Phys Chem B*. 2009;113:4571–7.
51. Yang C, Ishimoto K, Matsuura S, Koyasu N, Takahashi I. Depth-dependent inhomogeneous characteristics in supported glassy polystyrene films revealed by ultra-low X-ray reflectivity measurements. *Polym J*. 2014;46:873–9.
52. Nguyen HK, Inutsuka M, Kawaguchi D, Tanaka K. Depth-resolved local conformation and thermal relaxation of polystyrene near substrate interface. *J Chem Phys*. 2017;146:203313.
53. Ogawa Y, Lee CM, Nishiyama Y, Kim SH. Absence of sum frequency generation in support of orthorhombic symmetry of α -chitin. *Macromolecules*. 2016;49:7025–31.
54. Lee CM, Mohamed NMA, Watts HD, Kubicki JD, Kim SH. Sum-frequency-generation vibration spectroscopy and density functional theory calculations with dispersion corrections (DFT-D2) for cellulose I α and I β . *J Phys Chem B*. 2013;117:6681–92.

55. Rocha-Mendoza I, Yankelevich DR, Wang M, Reiser KM, Frank CW, Knoesen A. Sum frequency vibrational spectroscopy: The molecular origins of the optical second-order nonlinearity of collagen. *Biophys J*. 2007;93:4433–44.
56. Johnson CM, Sugiharto AB, Roke S. Surface and bulk structure of poly-(lactic acid) films studied by vibrational sum frequency generation spectroscopy. *Chem Phys Lett*. 2007;449:191–5.
57. Kusanagi H, Takase M, Chatani Y, Tadokoro H. Crystal structure of isotactic poly(4-methyl-1-pentene). *J Polym Sci Polym Phys*. 1978;16:131–42.
58. Masunaga H, Ogawa H, Takano T, Sasaki S, Goto S, Tanaka T, et al. Multipurpose soft-material SAXS/WAXS/GISAXS beamline at SPring-8. *Polym J*. 2011;43:471–7.
59. Ogawa H, Masunaga H, Sasaki S, Goto S, Tanaka T, Seike T, et al. Experimental station for multiscale surface structural analyses of soft-material films at SPring-8 via a GISWAX/GIXD/XR-integrated system. *Polym J*. 2013;45:109–16.
60. Sun H, Mumby SJ, Maple JR, Hagler AT. An ab initio cff93 all-atom force field for polycarbonates. *J Am Chem Soc*. 1994;116:2978–87.
61. Heinz H, Lin T-J, Kishore Mishra R, Emami FS. Thermodynamically consistent force fields for the assembly of inorganic, organic, and biological nanostructures: The interface force field. *Langmuir*. 2013;29:1754–65.
62. Takayanagi M, Kawasaki N. Mechanical relaxation of poly-4-methyl-pentene-1 at cryogenic temperatures. *J Macromol Sci Phys B*. 1967;1:741–58.
63. Hasegawa R, Tanabe Y, Kobayashi M, Tadokoro H, Sawaoka A, Kawai N. Structural studies of pressure-crystallized polymers. I. Heat treatment of oriented polymers under high pressure. *J Polym Sci Polym Phys*. 1970;8:1073–87.
64. De Rosa C, Borriello A, Venditto V, Corradini P. Crystal structure of form III and the polymorphism of isotactic poly(4-methylpentene-1). *Macromolecules*. 1994;27:3864–8.
65. De Rosa C. Chain conformation of form iv of isotactic poly(4-methyl-1-pentene). *Macromolecules*. 1999;32:935–8.
66. De Rosa C. Crystal structure of form ii of isotactic poly(4-methyl-1-pentene). *Macromolecules*. 2003;36:6087–94.
67. Mita K, Okumura H, Kimura K, Isaki T, Takenaka M, Kanaya T. Simultaneous small- and wide-angle X-ray scattering studies on the crystallization dynamics of poly(4-methylpentene-1) from melt. *Polym J*. 2012;45:79–86.
68. James Jebaseelan Samuel E, Mohan S. FTIR and FT raman spectra and analysis of poly(4-methyl-1-pentene). *Spectrochim Acta A*. 2004;60:19–24.
69. Ji N, Shen YR. Sum frequency vibrational spectroscopy of leucine molecules adsorbed at air-water interface. *J Chem Phys*. 2004;120:7107–12.
70. Kataoka S, Cremer PS. Probing molecular structure at interfaces for comparison with bulk solution behavior: Water/2-propanol mixtures monitored by vibrational sum frequency spectroscopy. *J Am Chem Soc*. 2006;128:5516–22.
71. Zhang C, Chen Z. Probing molecular structures of poly(dimethylsiloxane) at buried interfaces in situ. *J Phys Chem C*. 2013;117:3903–14.
72. Harp GP, Rangwalla H, Yeganeh MS, Dhinojwala A. Infrared-visible sum frequency generation spectroscopic study of molecular orientation at polystyrene/comb-polymer interfaces. *J Am Chem Soc*. 2003;125:11283–90.